Influence mechanism of electromagnetic absorbing metastructure anisotropy on radar cross section*

AN Qing[1], LIAO Wenhe[1], LI Dawei[1], LIU Tingting[1], LI Weiping[1], ZHANG Sen[2], ZHAO Junming[2]

1.School of Mechanical Engineering, Nanjing University of Science and Technology, Nanjing 210094, China

2.School of Electronic Science and Engineering, Nanjing University, Nanjing 210023, China

Abstract

To reveal the correlation between the anisotropy of electromagnetic absorbing metastructure and the radar cross section (RCS) of its curved components, the typical anisotropic hexagonal honeycomb (HH) metastructure and isotropic sheet gyroid (SG) metastructure are systematically studied. Both conformal mapping and non-conformal mapping methods are employed for designing the conformal curved components. These designs are compared using simulation and microwave anechoic chamber testing to evaluate their RCSs. The results indicate that the RCS of isotropic sheet gyroid curved components is insensitive to design methods, exhibiting strong design method and absorbing robustness; however, the RCS of anisotropic hexagonal honeycomb curved components exhibits strong dependence on design methods. Compared with anisotropic structures, metastructures with electromagnetic isotropy have significant advantages in achieving wide-angle and robust low-scattering characteristics of curved components, with lower dependence on design and processing. This study provides important design guidance for developing high-performance radar low-scattering components.

Graphical Abstract

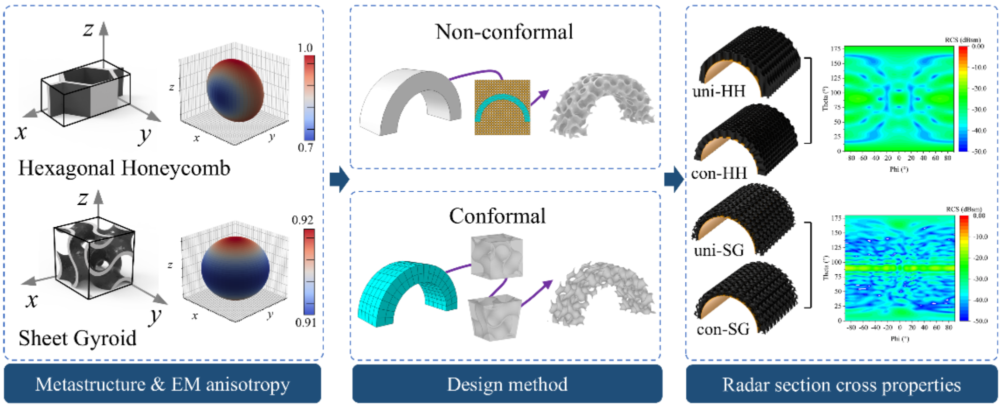

* The paper is an English translated version of the original Chinese paper published in Acta Physica Sinica. Please cite the paper as: **AN Qing1, LIAO Wenhe1 , LI Dawei1, LIU Tingting1, LI Weiping1, ZHANG Sen2, ZHAO Junming2, Influence mechanism of electromagnetic absorbing metastructure anisotropy on radar cross section.** *Acta Phys. Sin.*, 75(2): 020803. DOI: 10.7498/aps.75.20251200

DOI: 10.7498/aps.75.20251200

Keywords: electromagnetic absorbing metastructure, electromagnetic anisotropic, conformal design, additive manufacturing

DOI: 10.7498/aps.74.20251200
CSTR: 32037.14.aps.74.20251200

1 Introduction

Electromagnetic absorbing metastructures are multifunctional absorbers that integrate lightweight properties, load-bearing capacity, and broadband absorption. They have found extensive engineering applications[1-6], such as in aircraft wing leading edges and shielding walls of microwave anechoic chambers. Various fabrication techniques exist for electromagnetic absorbing metamaterials[7-9]. Typical methods include composite-type absorbers fabricated via extrusion or lamination processes[10-12] and coating-type absorbers produced through surface dip-coating or sputtering techniques[13-16]. The angular sensitivity of electromagnetic absorbing metastructure is closely related to the geometric configuration of their unit cells[17]. For instance, hexagonal honeycomb (HH) metastructures exhibit pronounced electromagnetic anisotropy, resulting in varying absorption performance under different incident angles. Consequently, conformal curved components based on HH metastructures demonstrate significant directional dependence in their radar cross section (RCS) across different observation angles.

Achieving low RCS over a wide angular domain in macroscopic structures requires consistent electromagnetic loss performance for waves incident from all directions. The core challenge lies in elucidating the intrinsic relationship between the electromagnetic anisotropy of absorbing metastructural unit cells and the RCS of macroscopic components. Prior studies have investigated the electromagnetic anisotropy of HH metastructures[18-20]. For example, Choi and Kim[18] compared the electromagnetic absorption performance of HH metastructures along transverse and axial directions. They fabricated HH metastructures by dip-coating glass/epoxy resin with multi-walled carbon nanotube coatings. Their measurements revealed superior absorption along the axial direction compared to the transverse direction. He et al.[19] employed strong perturbation theory to analyze the anisotropic effective electromagnetic properties of HH metastructures. They found that both effective permittivity and permeability increase with absorber thickness. By optimizing these parameters to approach each other, they guided impedance-matching design for honeycomb metastructures. Additionally, Yao et al.[20] examined the electromagnetic absorption characteristics of sheet gyroid (SG) metastructures along different cubic lattice orientations and experimentally validated their findings. Their results demonstrated excellent electromagnetic isotropy of SG metastructures across all three lattice directions.

To enhance the design robustness of low-RCS components, this study investigates the correlation between the electromagnetic anisotropy of metastructural unit cells and the RCS of macroscopic components, thereby identifying suitable electromagnetic absorbing metastructural types for low-RCS applications. Specifically, we selected the anisotropic HH metastructure and the isotropic SG metastructure as research subjects. Using electromagnetic simulation software, we compared absorption performance along three principal axes to quantify the anisotropy of unit-cell absorption. Furthermore, we employed conformal and non-conformal mapping design methods to fill curved components with HH and SG metastructures. Numerical analyses and fabrication tests were conducted on these curved components to evaluate their RCS. The results indicate that isotropic electromagnetic absorbing metastructures maintain stable absorption performance across all incident directions during both design and manufacturing, demonstrating strong robustness in absorption capability. This finding provides critical guidance for improving the robustness of omnidirectional low-RCS component design.

2 Unit Cell and Component Design

2.1 Unit Cell Design

This study focuses on two representative electromagnetic absorbing metastructures: HH and SG. Figures 1(a) and 1(b) illustrate the geometric features and structural compositions of these two unit cells. Each metastructure consists of a surface lossy material and a base structural framework. The HH unit cell dimensions are length $l = 17.4\text{mm}$, width $w = 10\text{mm}$, and height $h = 15\text{mm}$. The SG unit cell is cubic, with $l = w = h = 15\text{mm}$. Both unit cells have a volume fraction of $\rho = 0.1$. We modeled the SG unit cell using an implicit modeling approach, governed by the implicit equation shown in Equation (1):

$$\text{SG} = U^2 - C^2 \tag{1}$$

where, C and U denote the isosurface offset coefficient and the isosurface parameter term, respectively, as defined in Equations (2) and (3):

$$C = (\rho + 0.0149)/0.6816 \tag{2}$$

DOI: 10.7498/aps.75.20251200

$$U = \cos\left(2\pi\frac{x}{l}\right)\sin\left(2\pi\frac{y}{l}\right) + \cos\left(2\pi\frac{y}{l}\right)\sin\left(2\pi\frac{z}{l}\right) + \cos\left(2\pi\frac{z}{l}\right)\sin\left(2\pi\frac{x}{l}\right). \quad (3)$$

Equation (2) represents the relationship between the volume fraction ρ and the isosurface offset coefficient C. The wall thickness of the Schwarz P (SG) unit cell exhibits a positive correlation with its volume fraction. Equation (3) determines the size of the SG unit cell, where l denotes the unit cell dimension. The design domain of the metastructure has length, width, and height denoted by x, y, and z, respectively. Consequently, x/l, y/l, and z/l represent the number of unit cells along the three orthogonal directions.

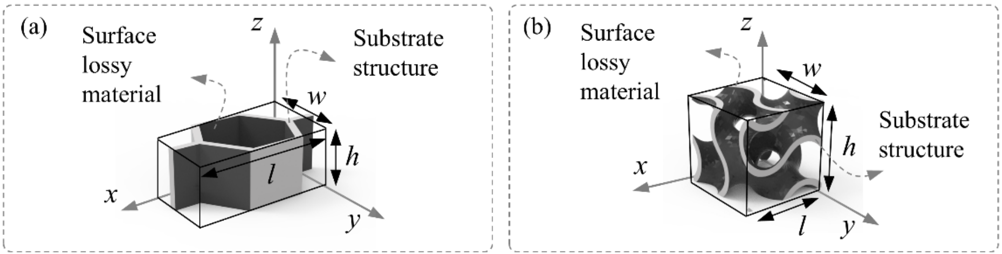

Fig. 1 (a) Hexagonal honeycomb metastructure unit; (b) sheet gyroid metastructure unit.

2.2 Design Method for Metastructural Curved Components

Conventional design approaches for electromagnetic wave-absorbing metastructural curved components employ non-conformal mapping methods. These methods yield metastructural unit cells on the curved component that exhibit pronounced anisotropy across different orientations. Consequently, the monostatic radar scattering performance of such curved components demonstrates poor consistency over wide angular domains. Figure 2(a) illustrates the non-conformal mapping design approach. In the Cartesian coordinate system, a metastructure design space Ω_1 is established by arraying along three orthogonal directions. The target curved component Ω_1 is then positioned within this metastructure design space. A non-conformal mapped curved component is obtained through a Boolean intersection operation ($\Omega_1 \cap \Omega_2$). In this resulting non-conformal mapped curved component, the normal vectors of all metastructural unit cells align in the same direction. Therefore, the radar cross section (RCS) of the curved component under incidence from various directions is closely tied to the angular sensitivity of the metastructural unit cells.

Compared with non-conformal mapping methods, conformal mapping effectively preserves the alignment of unit structures within filled curved components and maintains consistency with the surface curvature distribution. As illustrated in Figure 2(b), this method first discretizes the curved component into a finite element mesh composed of hexahedral elements. The geometric quality of this mesh is a critical factor determining whether the mapping retains conformality[21]. On this basis, shape functions N_i describe each hexahedral element of the curved component. Depending on the geometric configuration of the hexahedral elements, the shape functions fall into four distinct categories:

For cases where ζ_i, η_i, and ξ_i are all non-zero:

$$N_i = \frac{1}{8}(1+\zeta_i\zeta)(1+\eta_i\eta)(1+\xi_i\xi)\times(\zeta_i\zeta+\eta_i\eta+\xi_i\xi-2) \tag{4}$$

For $\zeta_i = 0$:

$$N_i = \frac{1}{4}(1-\zeta^2)(1+\eta_i\eta)(1+\xi_i\xi) \tag{5}$$

For $\eta_i = 0$:

$$N_i = \frac{1}{4}(1+\zeta_i\zeta)(1-\eta^2)(1+\xi_i\xi) \tag{6}$$

For $\xi_i = 0$:

$$N_i = \frac{1}{4}(1+\zeta_i\zeta)(1+\eta_i\eta)(1-\xi^2) \tag{7}$$

where, ζ_i, η_i, and ξ_i denote the local coordinates of the eight nodes within the metastructural element. Based on the shape of each hexahedral element in the curved component, the metastructural element undergoes a geometric transformation. Using the conformal mapping method described in Equation (8), the coordinates of the metastructural element are mapped to those of the hexahedral element, yielding the conformal-mapped element metastructure for the curved component. Sequentially filling all such metastructures ultimately produces the conformally mapped curved component:

$$(x,y,z)\left\{\begin{aligned} x &= \textstyle\sum_{i=1}^{8} N_i x_i \\ y &= \textstyle\sum_{i=1}^{8} N_i y_i \\ z &= \textstyle\sum_{i=1}^{8} N_i z_i \end{aligned}\right\}\ (i=1,2,\cdots,8) \tag{8}$$

where, x_i, y_i, and z_i denote the coordinates of the eight nodes of the hexahedron in the global coordinate system.

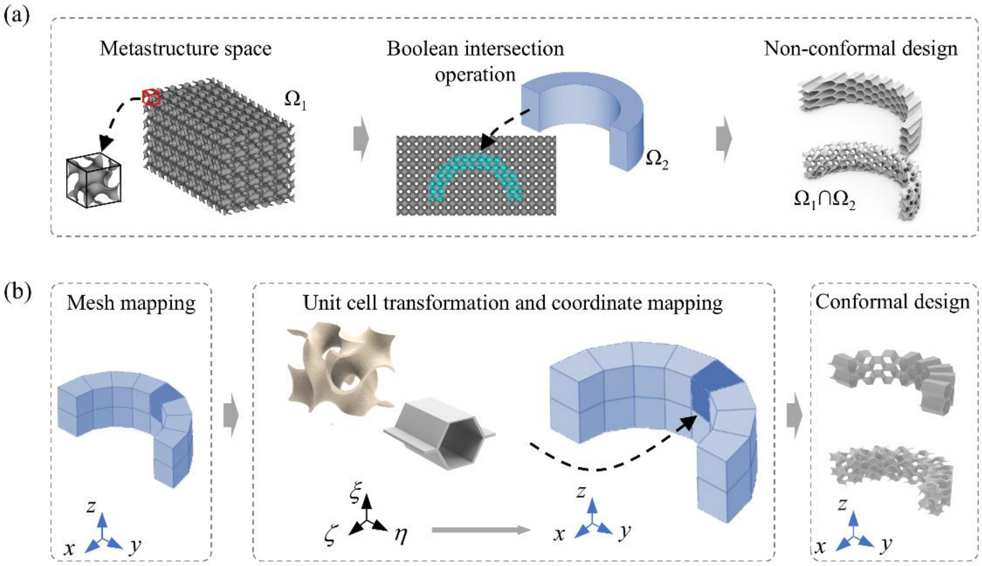

Fig. 2 Design method for electromagnetic absorbing metastructure curved component: (a) Non-conformal transformation method; (b) conformal transformation method.

3 Electromagnetic Anisotropy Analysis of the Metastructure

3.1 Anisotropy Analysis of Electromagnetic Absorption Performance

To investigate the electromagnetic absorption anisotropy of the HH and SG electromagnetic absorbing metastructure, we analyzed their absorption performance under electromagnetic wave incidence along three orthogonal directions, following the simulation setup illustrated in Fig. 4(a). The boundary conditions for the electromagnetic absorbing metastructures were set to "Unit cell." The boundary condition in the +*z* direction was configured as "Open (add space)," while that in the -*z* direction was set to "Electric (E_t = 0)." A frequency-domain solver was employed with a Gaussian excitation source. To ensure consistent thickness of the HH and SG metastructures along the direction of electromagnetic wave incidence, both were uniformly set to a thickness of h = 15 mm. The base material of the metastructures was acrylonitrile butadiene styrene (ABS), which has a dielectric constant of 2.96 and a loss tangent of 0.03. Through electromagnetic parameter fitting, the dispersive dielectric constant values of the material were obtained across the 2-18 GHz frequency range. Additionally, the permeability of the ABS material was set with a real part of 1 and an imaginary part of 0. The surface loss material exhibits resistive characteristics; thus, it was modeled as a surface resistance (ohmic sheet). Furthermore, we examined the influence of varying surface resistances on electromagnetic absorption performance, with results presented in Fig. 3. For the HH electromagnetic absorbing metastructures, the widest frequency bandwidth with

DOI: 10.7498/aps.75.20251200

reflection loss below -10 dB occurs within the surface resistance range of R = 700-800 Ω/sq. Similarly, for the SG electromagnetic absorbing metastructure, the broadest bandwidth with reflection loss below -10 dB is achieved when R = 600-800 Ω/sq. Based on this comprehensive simulation analysis, we selected R = 750 Ω/sq as the surface resistance for the metastructures. For electromagnetic absorbing metastructures backed by a metallic plate, the electromagnetic wave transmittance is zero. The relationship between electromagnetic absorption A and reflection loss (RL) is given by $A = 1 - R$, where $R = 10^{(RL/10)}$.

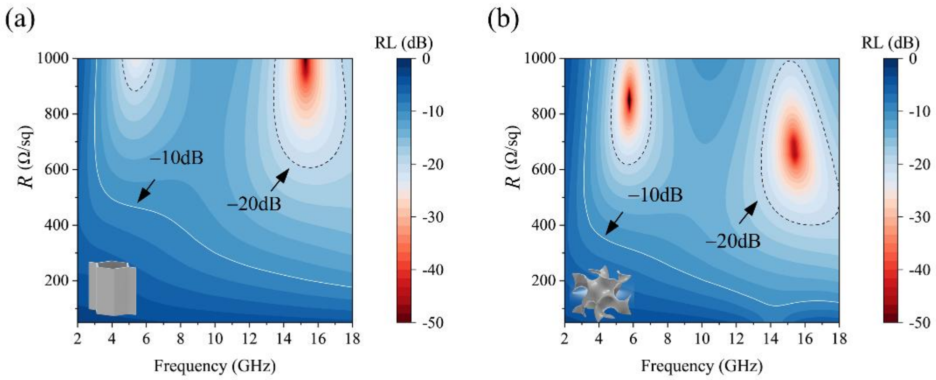

Fig. 3 Effect of surface resistance on RL for (a) the HH electromagnetic absorbing metastructure and (b) SG electromagnetic absorbing metastructure.

Figures 4(b) and 4(c) present the electromagnetic absorption rates of the HH and SG electromagnetic absorbing metastructures along the *x*, *y*, and *z* directions, respectively. The HH metastructure exhibits substantial differences in electromagnetic wave absorption between the *y*-axis and the *x*- and *z*-axes, with a difference of 10% at 5.5 GHz in particular. Additionally, the absorption rate along the *z*-axis surpasses that along the *x*-axis. For the SG metastructure, the absorption rates along all three orthogonal directions remain identical across the 2-10 GHz frequency band, although the rate along the *y*-axis is slightly lower than those along the other directions.

We substituted the simulated reflection coefficient S_{11} and transmission coefficient S_{21} into Equation (9) to calculate the refractive index of the electromagnetic absorbing metastructure. Subsequently, we employed the refractive index ellipsoid model described in Equation (10) to evaluate the electromagnetic anisotropy of the HH and SG metastructures. For biaxial anisotropic media, the principal refractive indices n_1, n_2, and n_3 are all unequal; conversely, for isotropic media, n_1, n_2, and n_3 are equal[22-25].

$$n = n' - jn'' = \frac{1}{d} \cdot \frac{c}{\omega} \cdot \cos^{-1} \frac{1 - S_{11}^2 + S_{21}^2}{2S_{11}} \quad (9)$$

$$\frac{x^2}{n_1^2}+\frac{y^2}{n_2^2}+\frac{z^2}{n_3^2}=1 \quad (10)$$

where, n, n', and n'' denote the refractive index, the real part of the refractive index, and the imaginary part of the refractive index, respectively; d represents the thickness of the metastructure; c denotes the speed of light; ω represents the angular frequency; and n_1, n_2, and n_3 correspond to the refractive indices along the *x*, *y*, and *z* directions of the refractive index ellipsoid, respectively.

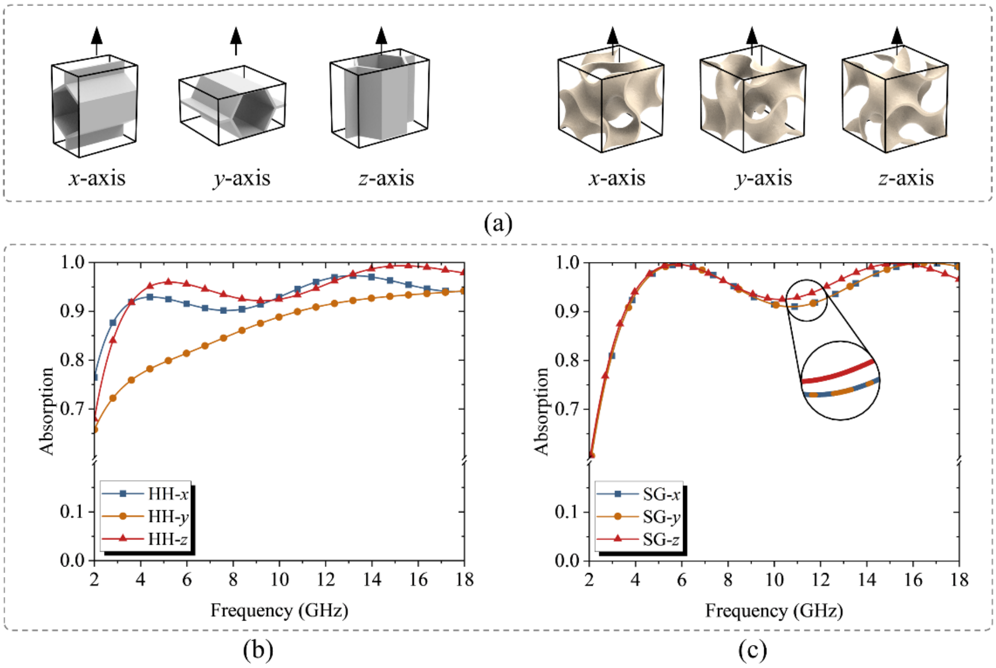

Fig. 4 The electromagnetic isotropy analysis: (a) The incident directions; (b) absorptivity of the HH electromagnetic absorbing metastructure; (c) the SG electromagnetic absorbing metastructure under the *x*-direction, *y*-direction, and *z*-direction.

Figures 5(a) and 5(b) illustrate the refractive index ellipsoid models of the HH and SG metastructures at 5.5 GHz and 16 GHz, respectively. For the HH metastructure, the maximum and minimum refractive indices at 5.5 GHz are 5.35 and 4.61 (a difference of 0.74), with the highest refractive index observed along the *z* direction. As the frequency increases to 16 GHz, the refractive index difference decreases slightly, with maximum and minimum values of 2.84 and 2.13, respectively (a difference of 0.71). Figures 5(c) and 5(d) present the refractive index ellipsoid models of the SG metastructure at 5.5 GHz and 16 GHz, respectively. With increasing frequency, the refractive index of the SG metastructure gradually decreases. In contrast to the HH metastructure, the differences between the maximum and minimum refractive indices for the SG metastructure at both 5.5 GHz and 16 GHz are less than 0.01. Based on the absorption spectra and refractive index ellipsoid models of the electromagnetic absorbing metastructures, the results indicate that the HH metastructure exhibits

DOI: 10.7498/aps.75.20251200

pronounced electromagnetic anisotropy, whereas the SG metastructure demonstrates electromagnetic isotropy.

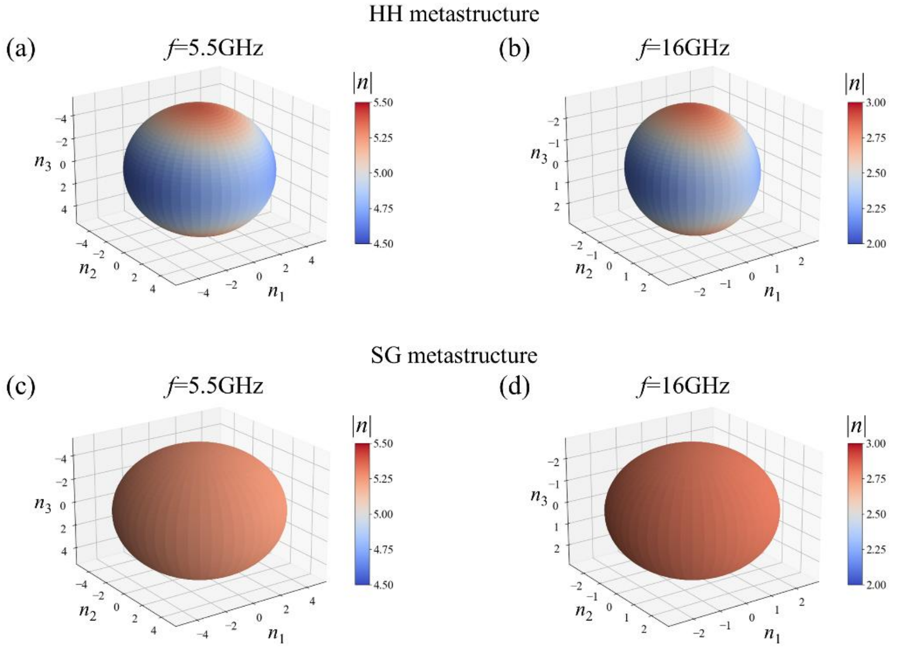

Fig. 5 Refractive index ellipsoid model: HH metastructure at (a) 5.5 GHz and (b) 16 GHz; SG HH metastructure at (c) 5.5 GHz and (d) 16 GHz.

3.2 Analysis of Electromagnetic Absorption Mechanisms

As shown in Figure 6(a), the HH metastructure excites strong magnetic resonances internally when electromagnetic waves are incident along the HH-*x* and HH-*z* directions, particularly near the frequency points of 5.5 GHz and 16 GHz. These resonances correspond directly to the high absorption peaks observed in Figure 4(b). In contrast, when electromagnetic waves are incident along the HH-*y* direction, effective magnetic resonances fail to form within the unit cell, leading to a significant reduction in absorption performance. This phenomenon clearly illustrates the origin of its anisotropic electromagnetic response, confirming that the HH metastructure exhibits pronounced anisotropic electromagnetic absorption characteristics. Figure 6(b) presents the magnetic field distributions of the SG metastructure along the *x*, *y*, and *z* directions. The magnetic field distributions are consistent across all three directions; for instance, at 5.5 GHz, strong magnetic resonances in all three orientations are primarily concentrated in the upper region of the metastructure. In summary, the magnetic field distribution characteristics of both the HH and SG metastructures align with the absorption spectra shown in Figures 4(b) and 4(c). The isotropic SG metastructure demonstrates uniform magnetic resonances along orthogonal directions,

DOI: 10.7498/aps.75.20251200

whereas the HH metastructure exhibits significant anisotropic electromagnetic properties, with markedly different magnetic resonances along the three orthogonal axes.

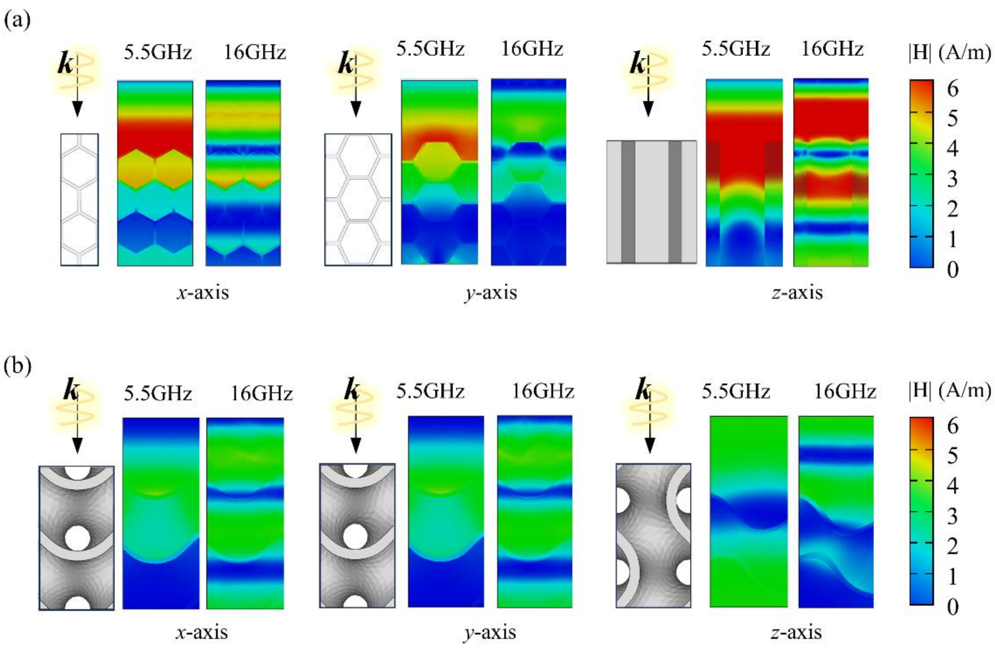

Fig. 6 Electromagnetic absorbing metastructure at magnetic field under the *x*-, *y*-, and *z*-direction: (a) HH; (b) SG.

4 Radar Cross Section Simulation and Testing

4.1 Radar Cross Section Simulation of Curved Components

To verify differences in radar cross section (RCS) among curved components filled with different metastructural unit cells, we first designed HH metastructural curved components (uni-HH) and SG metastructural curved components (uni-SG) using a non-conformal mapping method. Subsequently, we designed HH metastructural curved components (con-HH) and SG metastructural curved components (con-SG) using a conformal mapping method. Figure 7(a) shows the four metastructural curved components. The inner and outer radii of these curved components are r_1 = 75 mm and r_2 = 90 mm, respectively, with a metastructural unit cell thickness of 15 mm, as illustrated in Figure 7(a, I). A frequency-domain solver was employed to analyze the RCS of these four metastructural curved components.

Figures 7(b) and 7(c) analyze the radar cross section (RCS) of con-HH and uni-HH curved components, as well as con-SG and uni-SG curved components, at a frequency of 5.5 GHz. Theta (θ) and Phi (φ) denote the pitch and roll angles of the curved components, respectively, with the angular definitions illustrated in Figure 7(a, II). At

DOI: 10.7498/aps.75.20251200

5.5 GHz, uni-HH and con-HH curved components exhibit significant RCS differences within the azimuthal range of φ = ±20° to ±90°. Specifically, the uni-HH curved component demonstrates a low-scattering region with RCS ≈ -40 dBsm in this angular interval. For SG metastructure, the RCS curves of the curved components obtained via non-conformal and conformal mapping methods are nearly identical, with RCS values closely matching across all tested angles. Figures 7(d) and 7(e) analyze the RCS of con-HH and uni-HH, as well as con-SG and uni-SG curved components, at 16 GHz. As frequency increases, the RCS exhibits pronounced fluctuations; thus, comparisons at 16 GHz focus primarily on the angular ranges of φ = -20 ° to +20 ° and θ = 75° to 100°. For HH metastructure, con-HH and uni-HH curved components show RCS differences within specific angular ranges. In contrast, for SG metastructure, the RCS of con-SG and uni-SG curved components remains largely consistent.

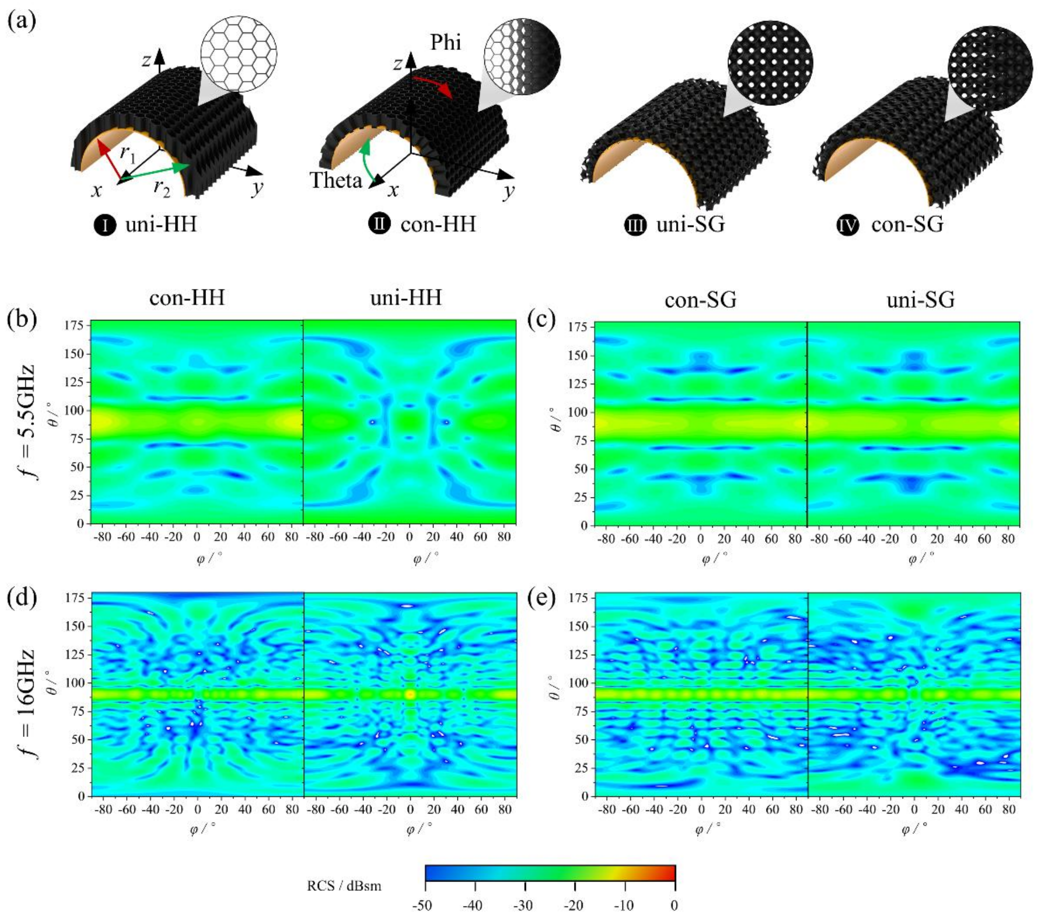

Fig. 7 (a) Curved component samples; radar cross section of (b) con-HH and uni-HH curved components and (c) con-SG and uni-SG curved components at 5.5 GHz; radar cross section of (d) con-HH and uni-HH curved components and (e) con-SG and uni-SG curved components at 16 GHz.

Figures 8(a) and 8(b) present the RCS difference curves between con-SG and uni-SG, as well as con-HH and uni-HH curved components, over the range of φ = -90 ° to +90 °

DOI: 10.7498/aps.75.20251200

at θ = 0°, for frequencies of 5.5 GHz and 16 GHz, respectively. At 5.5 GHz, regardless of whether non-conformal or conformal mapping is employed, the RCS variation of SG metastructural components with incident direction shows negligible differences. However, for HH metastructural components, the RCS variation with incident direction differs markedly between the two design methodologies. At higher frequencies (16 GHz), the sensitivity of RCS to the electromagnetic anisotropy of metastructural unit cells decreases across different incident directions on the curved components.

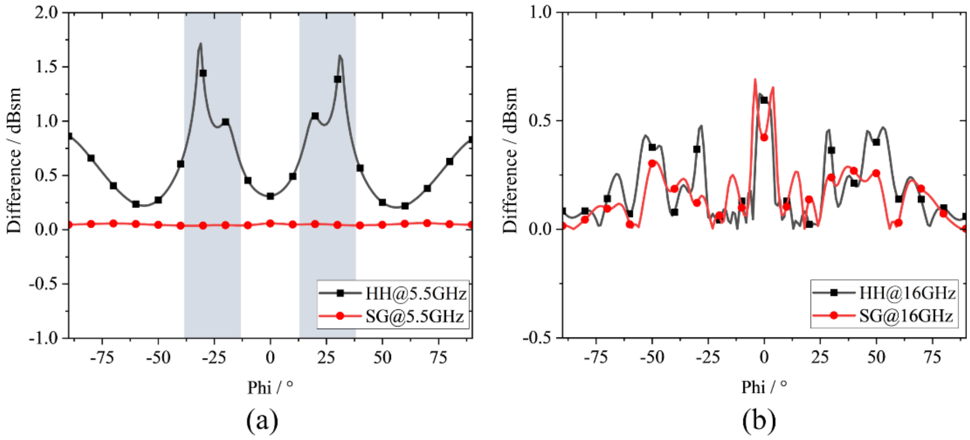

Fig. 8 Differential curves of RCS for non-conformal and conformal HH curved components and SG curved components at (a) 5.5 and (b) 16 GHz.

4.2 Fabrication of Curved Components and Radar Cross Section Testing

To validate the radar cross section (RCS) of curved components, we fabricated and tested these components. Figure 9(a) presents the fabrication process for both the metastructures and the curved components. First, we modeled the curved components using digital design software. Next, we employed a stereolithography-based 3D printer to fabricate the metastructure substrate structure, using acrylonitrile butadiene styrene (ABS, DaJian 8111X, DaJian Technology Co., Ltd., China) as the substrate material. We then applied a dip-coating process to the substrate surface to form a surface lossy material layer. This layer consisted of a mixture of carbon black powder and a curing solution. Finally, we bonded the dipped substrate structure to a metallic reflector plate to obtain the electromagnetic absorbing metastructure specimen. Figure 9(b) shows the curved components labeled con-HH, uni-HH, con-SG, and uni-SG, respectively. The dimensions of these fabricated components matched those of the simulation models described in Section 4.1. Figure 9(c) illustrates the testing configuration of the curved components inside a microwave anechoic chamber. We measured the RCS of the metastructural curved components over an angular range of ±90 °, covering the C-band (4-8 GHz) and Ku-band (12-18 GHz).

DOI: 10.7498/aps.75.20251200

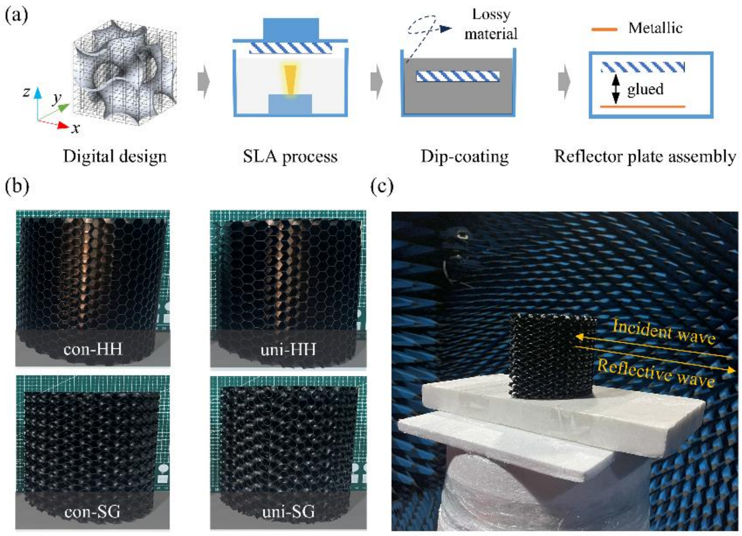

Fig. 9 Fabrication and testing: (a) The fabrication processing; (b) the con-HH, the uni-HH, the con-SG, and the uni-SG curved components; (c) the RCS testing scenario.

Figures 10(a) and 10(b) show the radar cross section (RCS) of the HH and SG curved components, respectively, at 5.5 GHz. Within the incident angle range of -90 °to +90 °, a significant RCS difference exists between the con-HH and uni-HH curved components. In contrast, the con-SG and uni-SG curved components exhibit a pronounced RCS difference only within the narrower range of -45 ° to +45 °. As the frequency increases to 16 GHz, the con-HH and uni-HH curved components display substantial RCS differences at incident angles of ±45 °, whereas the con-SG and uni-SG curved components yield nearly flat RCS curves, as illustrated in Figures 10(c) and 10(d).

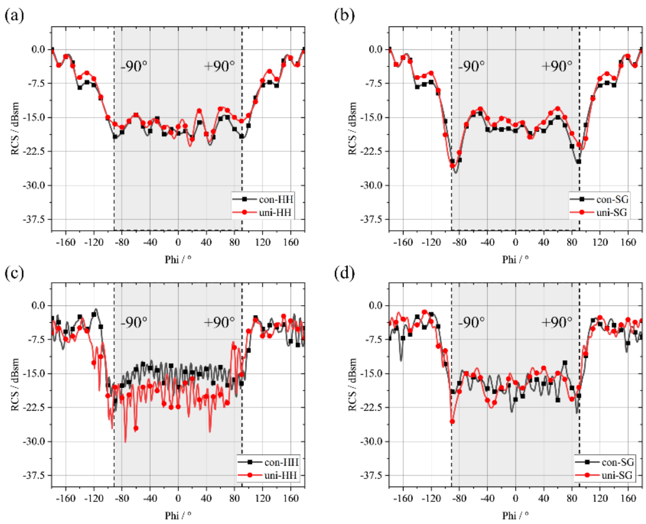

Fig. 10 RCS testing curves of the con-HH, con-SG, uni-HH, and uni-SG curved components at (a), (b) 5.5 GHz and (c), (d) 16 GHz.

DOI: 10.7498/aps.75.20251200

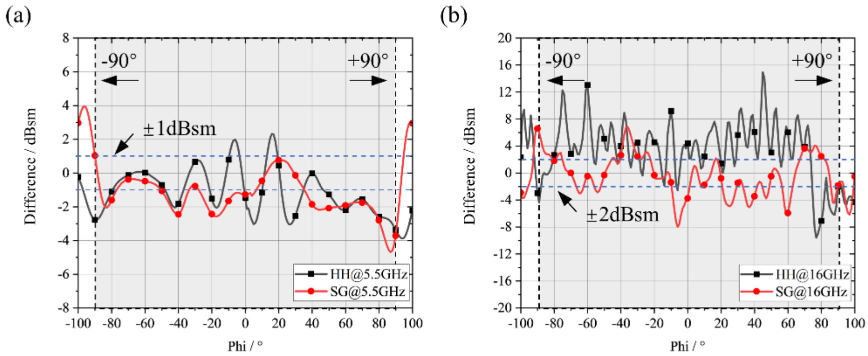

Fig. 11 The RCS difference of HH and SG curved components for (a) 5.5 GHz and (b) 16 GHz.

Furthermore, we performed interpolation calculations on the radar cross section (RCS) of curved components at the 5.5 GHz and 16 GHz frequency points, yielding the difference curves shown in Figures 11(a) and 11(b). We analyzed the discrepancies in RCS between the conformal mapping method and the non-conformal mapping method using the sample standard deviation (SSD), as expressed in Equation (11):

$$D = \sqrt{\frac{1}{n-1}\sum_{i=1}^{n}(x_i - \overline{x})^2} \tag{11}$$

where, $\overline{x}$ denotes the mean value of RCS; x_i represents the RCS data; n indicates the sample size. The difference value A is defined as the mean of the normalized standard deviation, as shown in Equations (12)-(13).

$$\mathrm{ND} = \frac{D_i - D_{min}}{D_{max} - D_{min}} \tag{12}$$

$$A = \frac{1}{m}\sum_{i=1}^{m}\mathrm{ND} \tag{13}$$

where, ND denotes the normalized standard deviation; D_{max} and D_{min} represent the maximum and minimum values of the standard deviation, respectively; S_i is each individual standard deviation value; and m is the number of RCS samples. Based on the above calculations, for the HH metastructure, the conformal and non-conformal mapping designs yield $A = 0.31$ at 5.5 GHz and $A = 0.24$ at 16 GHz. Similarly, for the SG metastructure, both designs produce $A = 0.28$ at 5.5 GHz and $A = 0.24$ at 16 GHz. Collectively, these results indicate that the SG structure exhibits superior robustness in absorption performance. Notably, the influence of metastructure anisotropy on the RCS of curved components demonstrates frequency dependence. At the lower frequency of 5.5 GHz (where the wavelength-to-structure ratio $\alpha = \lambda/h = 3.6$

DOI: 10.7498/aps.75.20251200

≈ 4), the design methodology-whether non-conformal or conformal mapping-significantly affects the RCS of HH curved components. In contrast, at the higher frequency of 16 GHz (α = 1.2 ≈ 1, where the structural dimensions are comparable to the wavelength), this design-induced difference diminishes. Analysis reveals that at higher frequencies, the shortened electromagnetic wavelength leads to more complex diffraction and scattering effects, which partially undermine the low-RCS characteristics primarily governed by the directional arrangement of macroscopic conformal mapping unit cells. Although discrepancies exist between measured and simulated results due to fabrication tolerances and environmental noise during testing, the measured trends align consistently with the simulation outcomes.

5 Analysis of Radar Scattering Differences Between Conformal and Non-Conformal Mapping Methods

To elucidate the differences in radar cross section (RCS) of curved components under varying incident angles, we comparatively analyze the magnetic field distribution characteristics of curved structures under normal-incidence electromagnetic waves. Figure 12 presents the magnetic field distributions of curved components at 5.5 GHz and 16 GHz under different incident angles. Specifically, Figure 12(a) shows the magnetic field distributions of con-HH, uni-HH, con-SG, and uni-SG curved components at 5.5 GHz and a 45° phase angle. At 5.5 GHz, the wavelength (approximately 54.5 mm) is significantly larger than the unit cell size of the metastructure (h = 15 mm), allowing the metastructure to be treated as an effective homogeneous anisotropic material. For the anisotropic HH metastructural curved components under normal-incidence electromagnetic waves, strong magnetic resonances in the con-HH component occur predominantly on the left and right sides, whereas the uni-HH component exhibits strong magnetic resonance at all angles. For the isotropic SG curved components under normal incidence, the strong magnetic resonance distributions of both con-SG and uni-SG components are identical, as highlighted within the black circles in Figure 12(a).

At 16 GHz, the wavelength (approximately 18.8 mm) becomes comparable to the unit cell dimension of the metastructure (h = 15 mm), causing localized scattering effects to become significant, as shown in Fig. 12(b). For the HH metastructure, the magnetic resonance distributions differ between the con-HH and uni-HH curved components: the con-HH component exhibits strong magnetic resonance at its base, whereas the uni-HH component shows strong magnetic resonance at its top. Similarly, for the SG electromagnetic absorbing metamaterial, the strong magnetic resonance regions differ between the con-SG and uni-SG curved components. Magnetic resonance coexists

DOI: 10.7498/aps.75.20251200

with electromagnetic resonance. By comparing the magnetic field distributions of the four curved components, we observe that, in the low-frequency band, the electromagnetic field characteristics of isotropic metastructural curved components are insensitive to (non-)conformal mapping methods. In contrast, in the high-frequency band, these characteristics become sensitive to (non-)conformal mapping methods, independent of the metastructure's anisotropy.

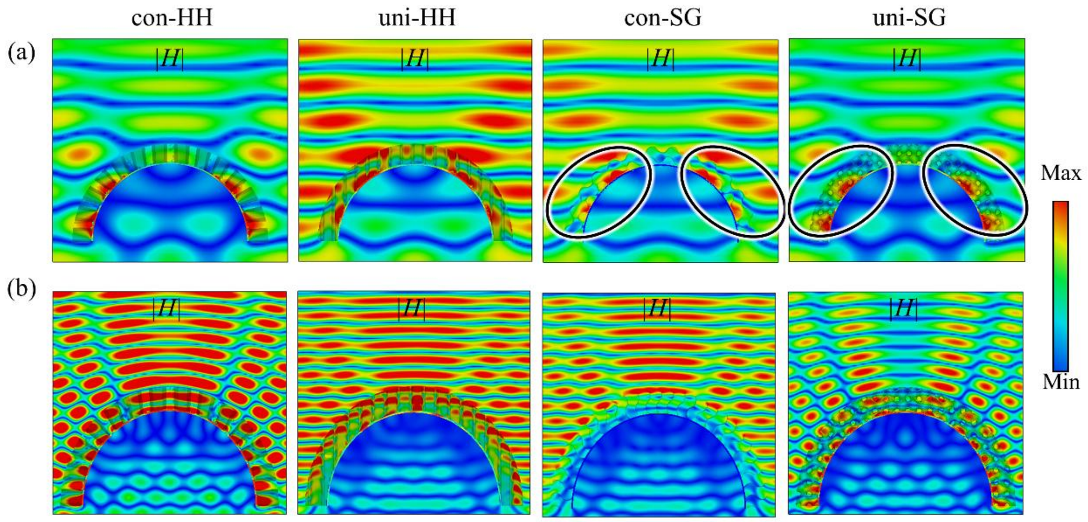

Fig. 12 Magnetic field distribution of con-HH, con-SG, uni-HH, and uni-SG (a) at 5.5 GHz with a phase of 45° and (b) at 16 GHz with a phase of 45°.

6 Conclusion

This study investigates the intrinsic relationship between the anisotropy of electromagnetic absorbing metastructure and the radar cross section (RCS) of their macroscopic components. We examine the magnetic field distributions and electromagnetic absorption characteristics of representative anisotropic hexagonal honeycomb and sheet gyroid metastructures under varying incident wave directions. Refractive index ellipsoid models at 5.5 GHz and 16 GHz are established, and electromagnetic numerical simulations elucidate the differences in electromagnetic anisotropy between the two structures. Curved components are designed using both conformal and non-conformal mapping methods, followed by RCS simulations and measurements. The RCS results indicate that the isotropic SG metastructural curved components exhibit insensitivity to the design methodology, demonstrating robust absorption performance. In contrast, the anisotropic hexagonal honeycomb curved components show strong dependence on the design method.

In summary, when designing components for wide-angle, low-RCS applications, isotropic electromagnetic absorbing metastructure, such as the sheet gyroid

DOI: 10.7498/aps.75.20251200

metastructure, exhibit robust absorbing performance. Conversely, when extreme electromagnetic absorbing is required for specific directions, anisotropic electromagnetic absorbing metastructure, such as the hexagonal honeycomb metastructure, can be employed. This research focuses on the macro-micro integrated electromagnetic behavior under single-curvature conditions. Future work may extend the electromagnetically isotropic sheet gyroid metastructure to complex curved component designs, providing theoretical foundations and engineering guidance for macro-micro integrated low-RCS component development.

References

[1] Wang Y Z, Xu H X, Wang C H, Wang M Z, Wang S J 2020 *Acta Phys. Sin.* **69** 134101

[2] Yang L X, Li Y B, Fei Q G 2025 *Acta Astronaut. Astronaut. Sin.* **46** 331808

[3] Mo M M, Ma W W, Pang Y Q, Chen R H, Zhang X M, Liu Z T, Li X, Guo W T 2018 *Acta Phys. Sin.* **67** 217801

[4] Zhou P H, Huang L R, Xie J L, Liang D F, Lu H P, Deng L J 2015 *IEEE Trans. Antennas Propag.* **63** 3496

[5] Gong P, Li Y, Xin C X, Chen Q Y, Hao L, Sun Q L, Li Z 2022 *Ceram. Int.* **48** 9873

[6] Li Z C, Xu J, Zhang L, Li Y W, Yang R S, Fu Q H, Zhang F L, Fan Y C 2023 *Ann. Phys.* **535** 2300054

[7] Zhang J H, Li D S, Wang M M 2025 *Addit. Manuf.* **97** 104613

[8] Zheng L, Niu L, Wang T, Li X C, Wang X, Gong R Z 2023 *Compos. Struct.* **305** 116464

[9] Xiong Y J, Wang Y, Wang Q, Wang C Q, Huang X Z, Zhang F, Zhou D 2018 *Acta Phys. Sin.* **67** 084202

[10] Bai L, Chang N, Zhao M Y, Hou C, Cao Y, Li D C 2024 *Chin. J. Aeronaut.* **37** 547

[11] Fan Q F, Yang X Z, Lei H S, Liu Y Y, Huang Y X, Chen M J 2020 *Composites Part A* **129** 105698

[12] Zhou Q, Qi C X, Shi T T, Li Y K, Ren W, Gu S Y, Xue B, Ye F, Fan X M, Du L F 2023 *Composites Part A* **169** 107541

[13] Lin Z M, Yu M M, Wen M L, Ma Z, Gao L H, Wang Y T, Chen W H, Chen G H, Ma C 2023 *Carbon* **214** 118389

[14] Ye F, Song Q, Zhang Z C, Li W, Zhang S Y, Yin X W, Zhou Y Z, Tao H W, Liu Y S, Cheng L F, Zhang L T, Li H J 2018 *Adv. Funct. Mater.* **28** 1707205

DOI: 10.7498/aps.75.20251200

[15]Luo H, Chen F, Wang X, Dai W Y, Xiong Y, Yang J J, Gong R Z 2019 *Composites Part A* **119** 1

[16]Kwak B S, Choi W H, Noh Y H, Jeong G W, Yook J G, Kweon J H, Nam Y W 2020 *Composites Part B* **191** 107952

[17]Xu J, Fan Y C, Su X P, Guo J, Zhu J X, Fu Q H, Zhang F L 2021 *Opt. Mater.* **113** 110852

[18]Choi W H, Kim C G 2015 *Composites Part B* **83** 14

[19]He Y F, Gong R Z, Wang X, Zhao Q 2008 *Acta Phys. Sin.* **57** 5261

[20]Yao L, Yang W Q, Zhou S X, Mei H, Li Y, Dassios K G, Riedel R, Liu C D, Cheng L F, Zhang L T 2023 *Acta Mater.* **249** 118803

[21]Fu J, Ding J H, Zhang L, Qu S, Song X, Fu M W 2023 *Addit. Manuf.* **62** 103406

[22]Tang X G, Zhang W H, Qiu K P 2013 *Acta Phys. Sin.* **62** 084102

[23]Gu Z Z, Chen L, Sun H M, Wang J P, Fan D G 2023 *2023 National Antenna Conference* Harbin, China, August 20, 2023 p. 2231

[24]Fan J Y, Zhang Y X, Feng X L, Huang Z X 2024 *Acta Phys. Sin.* **73** 244101 [Fan Jiu-Yang, Zhang Yu-Xian, Feng Xiao-Li, Huang Zhi-Xiang 2024 Acta Physica Sinica **73** 244101] Fan J Y, Zhang Y X, Feng X L, Huang Z X 2024 Acta Phys. Sin. 73 244101

[25]Xu S F, Sun Q 2013 *Adv. Aeronaut. Sci. Eng.* **4** 119

DOI: 10.7498/aps.75.20251200